# Directional electron transfer in single-atom cobalt nanozyme for enhanced photo-Fenton-like reaction

Shiang Liu [a,1], Yuwen Hu [a,1], Haojie Xu [a], Zhangrong Lou [b,*], Jianrong Chen [a], Cheng-Zong Yuan [c], Xingshuai Lv [c,*], Xiaoguang Duan [d], Shaobin Wang [d], Xi-Lin Wu [a,d,**]

[a] *College of Geography and Environmental Science, Zhejiang Normal University, Jinhua 321004, China*
[b] *Faculty of Medicine, Dalian University of Technology, Dalian 116024, China*
[c] *Institute of Applied Physics and Materials Engineering, University of Macau, Macao, PR China*
[d] *School of Chemical Engineering and Advanced Materials, The University of Adelaide, Adelaide, SA 5005, Australia*

## ARTICLE INFO

## ABSTRACT

In this study, enzyme-mimicking single-atom (EMSA) catalyst was fabricated by implanting cobalamin cofactor-resembling Co-N$_4$ sites into graphite carbon nitride (g-C$_3$N$_4$). The EMSA-Co sites inherit the high catalytic activity and selectivity from natural enzymes and demonstrate outstanding performance for persulfate (PS) activation under visible light (Vis). The kinetic rate constant for BPA degradation in the EMSA-Co-g-C$_3$N$_4$ +PS+Vis system was about 33 times faster than that in the g-C$_3$N$_4$+PS+Vis system. The benefits of high reactivity and selectivity of the EMSA-Co sites led to efficient generation of the radical species (SO$_4^{\bullet-}$, •OH and O$_2^{\bullet-}$), resulting in the fast elimination of various organic pollutants. Mechanisms studies reveal that the directional ultrafast electron transfer in the EMSA-Co nanozyme leads to an accelerated redox circulation of the Co single sites, thereby boosting their performance for photo-Fenton-like reaction. This study opens up the avenue of robust and efficient enzyme-like SACs for applications in environmental remediation.

## 1. Introduction

In recent years, advanced oxidation processes (AOPs) have been extensively studied for the purification of organic contaminants in wastewater. Among AOPs, sulfate radical (SO$_4^{\bullet-}$) is appealing because of the higher redox potential (2.5–3.1 V) [1,2], longer half-life (30–40 ms) and a wider applicable pH window (pH 3–11) than hydroxyl radical (•OH, 1.9–2.7 V, < 1 µs, pH 3–5) [3,4]. Persulfate (PS) and peroxymonosulfate (PMS) are the parent oxides of SO$_4^{\bullet-}$, which can be activated for degradation of pollutants with the assistance of various media such as light [5,6], ultrasound [7], heat [8] and transition metals [9,10]. However, these methods usually suffer from the low catalytic efficiency, high energy consumption, and inevitable introduction of secondary pollution by the metal catalysts. Heterogeneous activation of PS/PMS by using solid nanocatalysts is emerging for abatement of organic wastewater [11], owing to the advantages of easy separation and excellent stability and reusability of the nanocatalysts. Besides the heterogeneous Fenton-like reactions, the heterogeneous photo-Fenton-like reactions to enhance the catalytic performance for pollutants removal also have been developed in recent years [12]. For example, Avetta and co-workers reported the enhanced activation of PS by using magnetite nanoparticles under UVA irradiation [13]. Tian et al. found that the Fe$^{2+}$-mediated Fenton-like reactions were boosted by using WO$_3$ as co-catalysts under visible light [14]. Despite an increasing number of studies have explored the nanocatalysts mediated photo-Fenton-like reactions, the development of reactive and robust multifunctional catalysts are still challenging.

As emerging nanoscale catalysts, single atom catalysts (SACs) bridge the gap between homogeneous and heterogeneous catalysis [15,16], maximize the atomic utilization, and exhibit unique physical and chemical properties [17]. The atomically dispersed metal active sites supported by various substrates endow SACs with tunable activity, selectivity and durability [18], leading to satisfactory performances in various catalytic reactions [19–22]. Metalloenzymes with single-atom metal sites exhibit high catalytic activity and selectivity to catalyze fundamental redox reactions, such as N$_2$ fixation and O$_2$ reduction [23].

---

SACs by mimicking the active center of metalloenzymes, namely single-atom nanozyme, have been demonstrated to inherit the characteristics of natural enzymes and exhibit comparable catalytic activity and selectivity for biosensing and biotherapy [24,25]. In addition, loading single-atom nanozyme on catalytic support offers a unique opportunity to synthesize heterogeneous catalysts with multifunctional properties and enhanced performance. Bearing these in mind, synergistic coupling of single-atom nanozyme with photocatalytic substrates may reap the benefits of both photocatalysts and SACs and provides a new approach to fabricating robust and efficient enzyme-mimicking single-atom (EMSA) catalyst.

Herein, we designed and synthesized EMSA catalyst by embedding cobalamin cofactor-resembling Co-N$_4$ sites into photocatalytic graphitic carbon nitride (g-C$_3$N$_4$) via a facile copolymerization approach. The EMSA-Co sites on g-C$_3$N$_4$ (EMSA-Co-g-C$_3$N$_4$) exhibited an enhanced performance for the degradation of bisphenol A (BPA) via PS activation under visible light (Vis). Effects of the reaction conditions (solution pH, catalyst dosage and PS dosage) on BPA degradation by EMSA-Co-g-C$_3$N$_4$ mediated photo-Fenton-like reaction were systematically studied. The reactive oxygen species (ROS) were probed by quenching experiments and electron paramagnetic resonance (EPR). For the first time, we revealed that the EMSA-Co-g-C$_3$N$_4$ catalyst was able to guide and accelerate the transportation of photogenerated electrons from the g-C$_3$N$_4$ substrate to the surface Co catalytic sites, leading to enhanced production of ROS in the EMSA-Co-g-C$_3$N$_4$+PS+Vis system. This study provides a facile strategy for the fabrication of single-atom nanozyme and opens up a new avenue to applying enzyme-mimicking catalysts for environmental applications.

## 2. Materials and methods

### 2.1. Chemicals, characterizations and computational details

The chemicals are provided in **Text S1**, Supporting Information. Details for the characterization techniques and computational methods are shown in **Text S2** and **Text S4,** Supporting Information, respectively.

### 2.2. Preparation of the catalysts

For the synthesis of EMSA-Co-g-C$_3$N$_4$, 1.25 g of dicyandiamide (DCDA), 1.25 g of urea and a fixed amount of cobalamin were added into 40 mL of deionized water in an Erlenmeyer flask. The mixture was heated to 60 ℃ and stirred at 300 rpm to form a solid paste. After that, the mixture paste was dried in vacuum at 60 ℃ for 24 h. The dried mixture solids were then ground into powder and subjected to calcination for 2 h in a muffle furnace at the heating rate of 5 ℃ per minute. Finally, the product was cooled down to room temperature and the grey EMSA-Co-g-C$_3$N$_4$ was obtained under 550 ℃. The samples prepared by calcination of the mixture at 450 and 650 ℃ were denoted as Co-CN-450 and Co-CN-650. The pure g-C$_3$N$_4$ was prepared via the same procedure without adding cobalamin in the precursor. The cobalt content in EMSA-Co-g-C$_3$N$_4$ was adjusted by varying the mass ratio of cobalamin to DCDA in the precursor from 0.27 (0.25 mM), 0.54 (0.50 mM), 0.82 (0.75 mM) to 1.09 (1.0 mM). The Co-content in the various EMSA-Co-g-C$_3$N$_4$ samples were determined by inductively coupled plasma atomic emission spectrometer, which were 3.81%, 4.56%, 5.06% and 6.74 wt%, respectively.

### 2.3. Experimental procedure

The catalytic activity of the as-prepared EMSA-Co-g-C$_3$N$_4$ was evaluated using BPA as a model pollutant and PS as the oxidant. All experiments were performed in 100 mL beaker containing 30 mL of 40 mg/L BPA and 0.2 g/L of EMSA-Co-g-C$_3$N$_4$. First, the suspension was magnetically stirred for 60 min to achieve the adsorption-desorption equilibrium. Second, 0.015 g of PS was added into the above

suspension under continuous stirring, simultaneously by exposing the mixture to a simulated visible light (300 W Xe lamp with a piece of UV cutoff filter ($\lambda < 420$ nm)). At certain time intervals, 0.5 mL of the mixture was sampled and the solid catalysts were separated by centrifugation at 10000 rpm. The concentration of BPA in the supernatant was determined by HPLC. Degradation of various organic pollutants (rhodamine B (RhB), Meropenem (MEM) and tetrabromobisphenol A (TBBPA)) by using the EMSA-Co-g-C$_3$N$_4$+PS+Vis system were also studied following the similar procedure as described above. The degradation rates were calculated by (($C_0$–$C_t$)/$C_0$)$\times$ 100%, where $C_0$ is the initial concentration and $C_t$ is the concentration at sampling time. The test conditions of HPLC and UV-Vis for detection of the various organic pollutants were listed in Table S1. And the BPA degradation intermediates were detected by liquid chromatography tandem mass spectrometry (LC-MS/MS).

## 3. Results and discussion

### 3.1. Materials characterization

As shown in Fig. 1a, the EMSA-Co-g-C$_3$N$_4$ was synthesized by mimicking the active center of cobalamin-dependent methionine synthase [26]. The cobalamin cofactor resembling Co–N$_4$ single-sites were implanted into g-C$_3$N$_4$ by a facile copolymerization method. The scanning electron microscopy (SEM) image (Fig. S1) shows a two-dimensional sheet-like structure of EMSA-Co-g-C$_3$N$_4$ with a rough surface and abundant cracks/pores. Transmission electron microscope (TEM) images (Fig. S2) demonstrate the presence of abundant nanopores in EMSA-Co-g-C$_3$N$_4$, which facilitate the diffusion and transportation of reactants from aqueous solution to surface catalytic sites and speed up the reaction kinetics. High-angle annular dark-field scanning TEM (HAADF-STEM) (Fig. 1b and c) shows tiny bright spots with the size of 2–3 Å in the g-C$_3$N$_4$ substrate, corresponding to the atomically dispersed Co atoms. High-resolution TEM (HR-TEM) image (Fig. 1d) and the corresponding energy dispersive X-Ray spectroscopy (EDX) mapping images (Fig. 1e-g) illustrate the homogeneously distributed C, N and Co elements in EMSA-Co-g-C$_3$N$_4$. The X-ray diffraction (XRD) patterns of pure g-C$_3$N$_4$ and EMSA-Co-g-C$_3$N$_4$ show the typical diffraction peak located at 27.5° (Fig. 1h), which is assigned to the (002) plane of g-C$_3$N$_4$ [27,28]. The diffraction peaks of cobalt, cobalt oxide, cobalt nitride, and cobalt carbide are not observed, indicating that the cobalt may be atomically dispersed on g-C$_3$N$_4$.

X-ray photoelectron spectroscopy (XPS) was applied to investigate the elemental compositions of the samples. The dominant peaks of C, N and O elements were observed in the XPS spectra of both g-C$_3$N$_4$ and EMSA-Co-g-C$_3$N$_4$ (Fig. S3). A small peak for the Co element can be distinguished in the XPS spectrum of EMSA-Co-g-C$_3$N$_4$. From the high-resolution C1s XPS spectra (Fig. 1i), the peaks at 288.2 and 287.7 eV are attributed to the sp$^2$ carbons (N = C–N) of triazine rings and C-N in the g-C$_3$N$_4$ matrix, respectively [29,30]. As compared with pure g-C$_3$N$_4$, two new and prominent peaks at 286.4 and 284.8 eV, corresponding to the adventitious C-NH$x$ ($x$ = 1, 2) groups and conjugated carbons (C=C) [31], are observed in the C1s XPS spectrum of EMSA-Co-g-C$_3$N$_4$. These new carbon species resulting from the doped corrin ring may change the localized electronic structure of EMSA-Co-g-C$_3$N$_4$ [32], leading to improved light absorption and electrons/holes transportation. The N 1 s XPS spectrum of g-C$_3$N$_4$ shows the peaks at 398.5, 399.8 and 400.6 eV (Fig. 1j), attributing to pyridinic N, pyrrolic N (N-(C)$_3$) and graphitic N [12], respectively. From the N 1 s XPS spectrum of EMSA-Co-g-C$_3$N$_4$, the peaks located at 398.2 and 399.8 eV are assigned to pyridinic N and pyrrolic N, respectively. The peak intensity of pyrrolic N for EMSA-Co-g-C$_3$N$_4$ is much stronger than that for g-C$_3$N$_4$, owing to the incorporation of the corrin ring (pyrrole-type Co-N$_4$ sites) into the g-C$_3$N$_4$ matrix. The high-resolution Co 2p XPS spectrum of EMSA-Co-g-C$_3$N$_4$ shows the peaks for Co(II) (782.9 and 802.5 eV), Co (III) (780.8 and 796.6 eV) and the satellite peaks (786.2 and 807.3 eV)
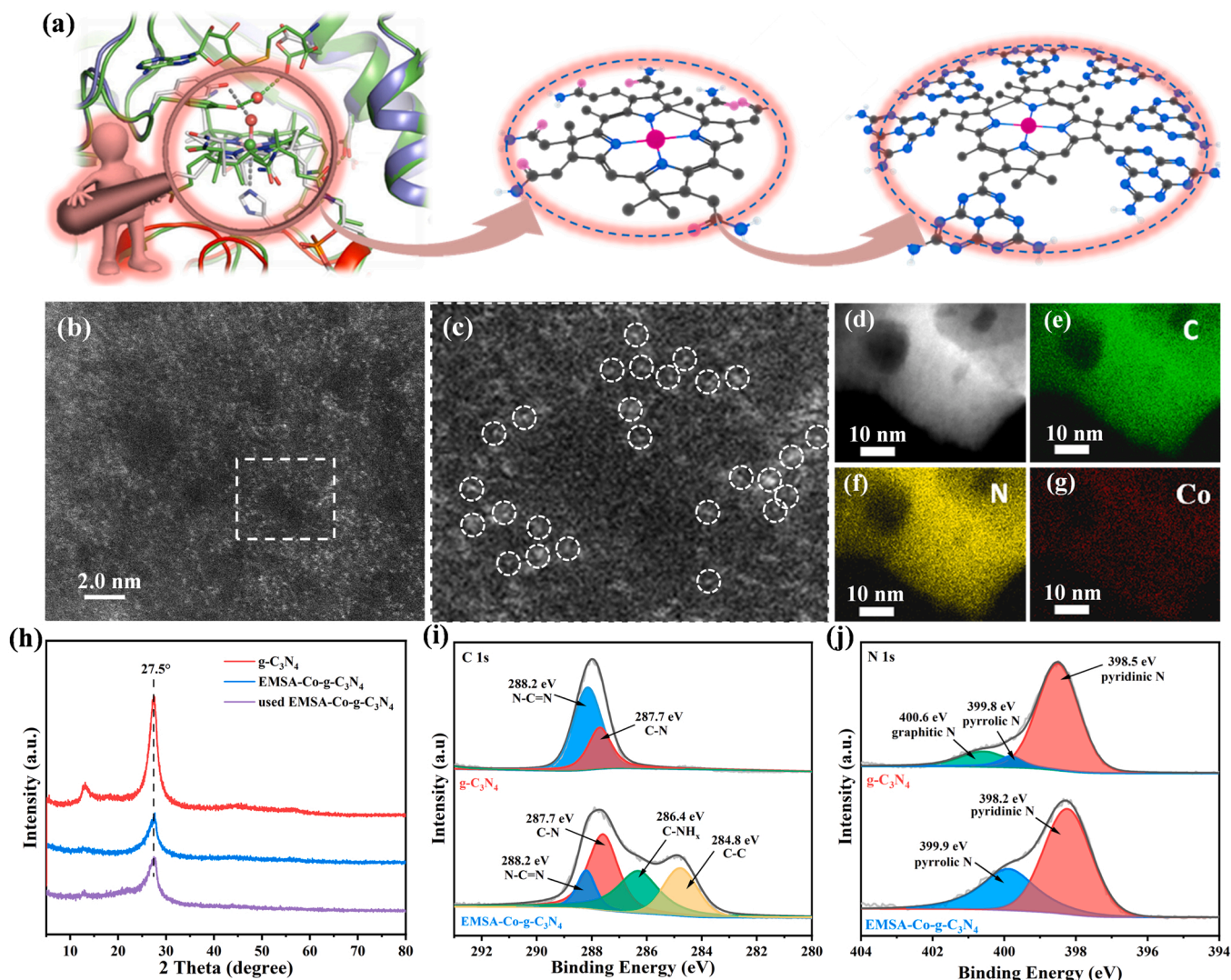
**Fig. 1.** (a) Schematic illustration of the fabrication of EMSA-Co-g-$C_3N_4$, (b) HAADF-STEM image, (c) the corresponding enlarged image of the selected area, (d) TEM image, and (e-g) the corresponding EDX mapping of EMSA-Co-g-$C_3N_4$, (h) XRD patterns of the samples, (i) C 1 s and (j) N 1 s XPS spectra of the g-$C_3N_4$ and EMSA-Co-g-$C_3N_4$.

(Fig. S4) [33–35]. The valence state and coordination structure of the Co single sites were further probed by extended X-ray absorption fine structure (EXAFS) measurements. Fig. 2a displays the Co K-edge X-ray absorption near edge structure (XANES) spectra of Co foil, $Co_3O_4$, phthalocyanine cobalt (CoPc), cobalamin and EMSA-Co-g-$C_3N_4$. Notably, the absorption edge of EMSA-Co-g-$C_3N_4$ is located between CoPc and $Co_3O_4$, implying the valence state of Co species is between Co (II) and Co(III). Fourier-transformed EXAFS profile of EMSA-Co-g-$C_3N_4$ (Fig. 2b) exhibits an obvious peak at ~1.37 Å due to the Co-N coordination at the first shell [36]. The absence of peaks for Co-Co bonds (~2.17 Å) further confirmed the atomic dispersion of Co species in EMSA-Co-g-$C_3N_4$ [37]. The EXAFS spectra of EMSA-Co-g-$C_3N_4$ are fitted in *R* (Fig. 2c) and *k* (Fig. 2d) spaces, and the corresponding fitting parameters are summarized in Table S2. The coordination number of the Co–N shell is 4.0 at a distance of 1.98 Å for EMSA-Co-g-$C_3N_4$, which are the same or close to the values for CoPc, demonstrating that the EMSA-Co-g-$C_3N_4$ well inherited the coordination structure of cobalamin that the Co atoms are coordinated with four N atoms (Co-$N_4$, insert in Fig. 2c). The EXAFS fitting for the Co foil, $Co_3O_4$ and CoPc are shown in Fig. S5 and the related fitting parameters are listed in Table S2. The results demonstrate that EMSA-Co-g-$C_3N_4$ and CoPc have similar coordination structures. Thus, the enzyme-mimicking single-atom Co

catalyst was successfully constructed by implanting the cobalamin cofactor-resembling Co-$N_4$ sites into the g-$C_3N_4$ framework.

From the UV–vis–NIR diffuse reflectance spectra (UV–vis–NIR DRS) (Fig. 2e), one can notice that EMSA-Co-g-$C_3N_4$ exhibits broader and stronger light absorption than pure g-$C_3N_4$, which leads to an improved light harvest [32]. From the plots of $(E_{photon})^{1/2}$ vs. $E_{photon}$ (inset in Fig. 2e), the bandgap decreases from 2.76 eV for g-$C_3N_4$ to 2.52 eV for EMSA-Co-g-$C_3N_4$. The narrower band gap of EMSA-Co-g-$C_3N_4$ is conducive to promoting the generation of photoexcited charge carriers. The implanted EMSA-Co dopants may create impurity energy levels between the valence band (VB) and conduction band (CB) of g-$C_3N_4$, which decreases the transition energies for photoexcited electrons [38]. The photoluminescence (PL) emission spectra show two prominent emission peaks at 440 and 468 nm (Fig. 2f), corresponding to the bandgap emission of carbon nitride. Compared with g-$C_3N_4$, EMSA-Co-g-$C_3N_4$ has lower PL intensity, suggesting improved charge carrier separation and suppressed charge carrier combination. The EMSA-Co dopants may provide extra trapping states (TSs) for capturing the photogenerated electrons, thus promoting the separation of the photogenerated charge carriers and restraining their recombination [39]. As shown in Fig. 2g, a singlet peak at about g = 2.004 was observed in the electron paramagnetic resonance (EPR) spectra of the samples, owing to
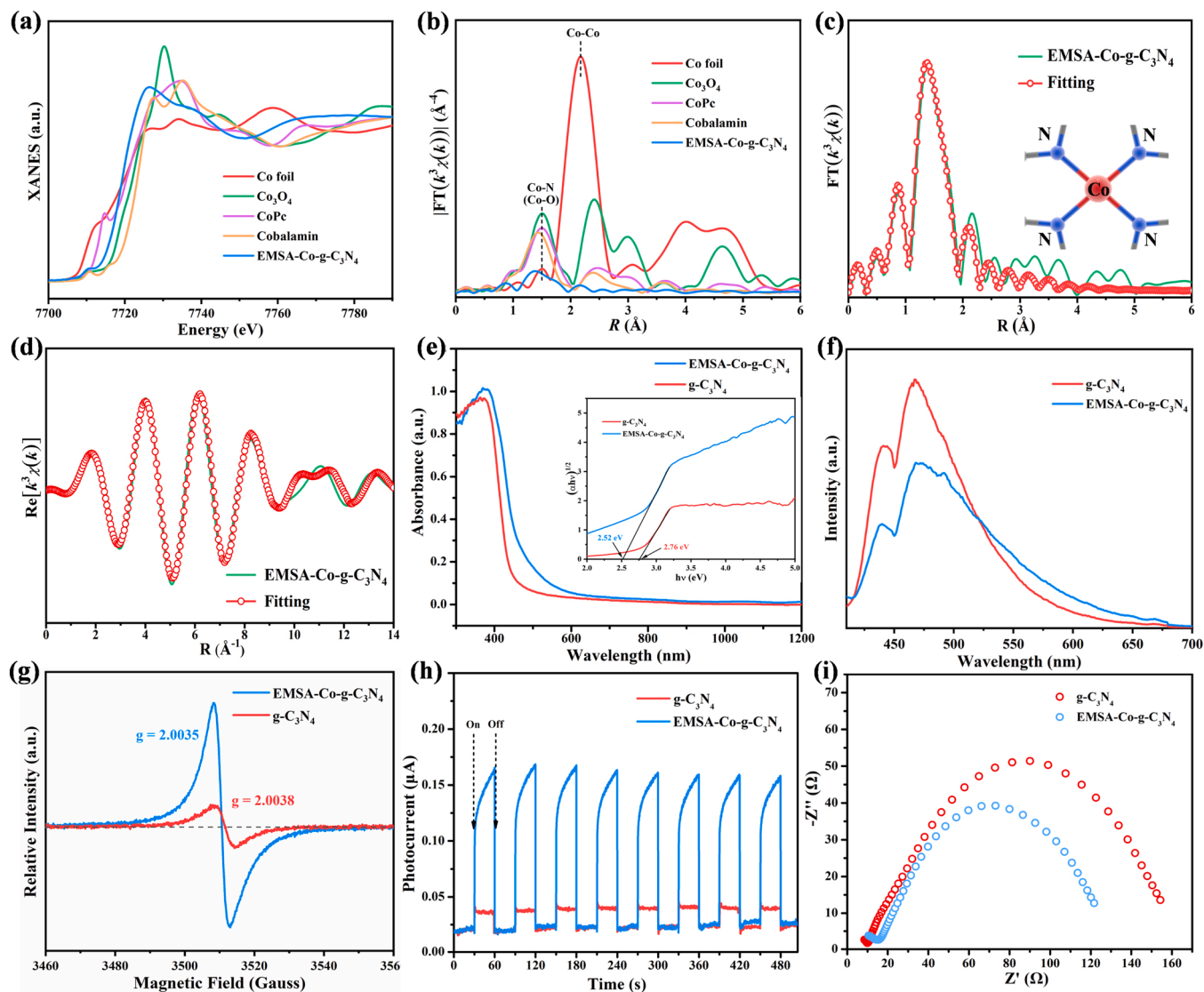
**Fig. 2.** (a) XANES spectra and (b) Fourier transform (FT) EXAFS spectra of the samples. EXAFS fitting curves of EMSA-Co-g-C$_3$N$_4$ at (c) R-space and (d) $\kappa$-space. (e) UV–vis–NIR diffuse repentance spectra (insert shows the plots of (E$_{photon}$)$^{1/2}$ vs. E$_{photon}$). (f) PL emission spectra, (g) EPR spectra, (h) photocurrent responses (i) EIS Nyquist plots of g-C$_3$N$_4$ and EMSA-Co-g-C$_3$N$_4$.

the unpaired electron on the aromatic carbon atoms [40]. The much higher peak intensity for EMSA-Co-g-C$_3$N$_4$ suggests the presence of more C-vacancies and defect sites, which are beneficial to improving its photocatalytic performance. In addition, as compared with pristine g-C$_3$N$_4$, the EMSA-Co-g-C$_3$N$_4$ shows much stronger photocurrent responses (Fig. 2h), confirming its enhanced photocatalytic properties. From the electrochemical impedance spectra (EIS) (Fig. 2i), EMSA--Co-g-C$_3$N$_4$ has a smaller arc radius in the Nyquist plots than g-C$_3$N$_4$, suggesting its lower interfacial charge transfer resistance to accelerating the electron transfer process for surface catalytic reactions.

### 3.2. Catalytic activation of persulfate

The performances of EMSA-Co-g-C$_3$N$_4$ for catalytic activation PS and PMS were studied (Fig. S6). It was found that the EMSA-Co-g-C$_3$N$_4$+PS+Vis system was more efficient for BPA oxidation than the EMSA-Co-g-C$_3$N$_4$+PMS+Vis system. Effect of calcination temperature of the catalyst for BPA degradation is shown in Fig. S7. The catalysts prepared at 450 and 650 °C (Co-CN-450 and Co-CN-650) exhibited much poorer performance for BPA degradation than EMSA-Co-g-C$_3$N$_4$. The catalysts were optimized by varying the cobalamin mass ratio of

cobalamin to DCDA in the precursors. As shown in Fig. S8, the EMSA-Co-g-C$_3$N$_4$ samples with 0.75 and 1.0 mM of Co in the precursor achieved the best performances with ~98.5% and 98.0% of BPA degradation, respectively. Similarly, the catalyst and PS dosages were optimized to be 0.2 and 0.5 g/L, respectively (Fig. S9 and S10). In Fig. 3a, one can observe that the EMSA-Co-g-C$_3$N$_4$+PS+Vis system maintains high removal efficiency (>96%) toward BPA over a wide pH range (pH3.0–11.0). The leached Co ions in the EMSA-Co-g-C$_3$N$_4$+PS+Vis system account for less than 1.5% of the total Co-content in EMSA-Co-g-C$_3$N$_4$ over all the tested pH range (Table S3). In addition (Fig. 3b), the removal percentages of BPA maintain over 90% after 5 successive cycles of the catalytic degradation processes, demonstrating the great reusability of EMSA-Co-g-C$_3$N$_4$. We further examined the used catalysts by XRD and XPS. The XRD patterns of the fresh and recycled EMSA-Co-g-C$_3$N$_4$ are almost identical (Fig. 1h), indicating that the structure and phase of EMSA-Co-g-C$_3$N$_4$ did not change in the catalytic oxidation reactions. From XPS spectrum of the recycled EMSA-Co-g-C$_3$N$_4$ (Fig. S4), prominent Co 2p$_{1/2}$ and Co 2p$_{3/2}$ peaks for Co(II) can be observed, implying the accelerated Co(II)/Co(III) cycles in photo-Fenton-like reactions. The EMSA-Co-g-C$_3$N$_4$+PS+Vis system was efficient for the oxidation of various organic pollutants (Fig. S11), including MEM,
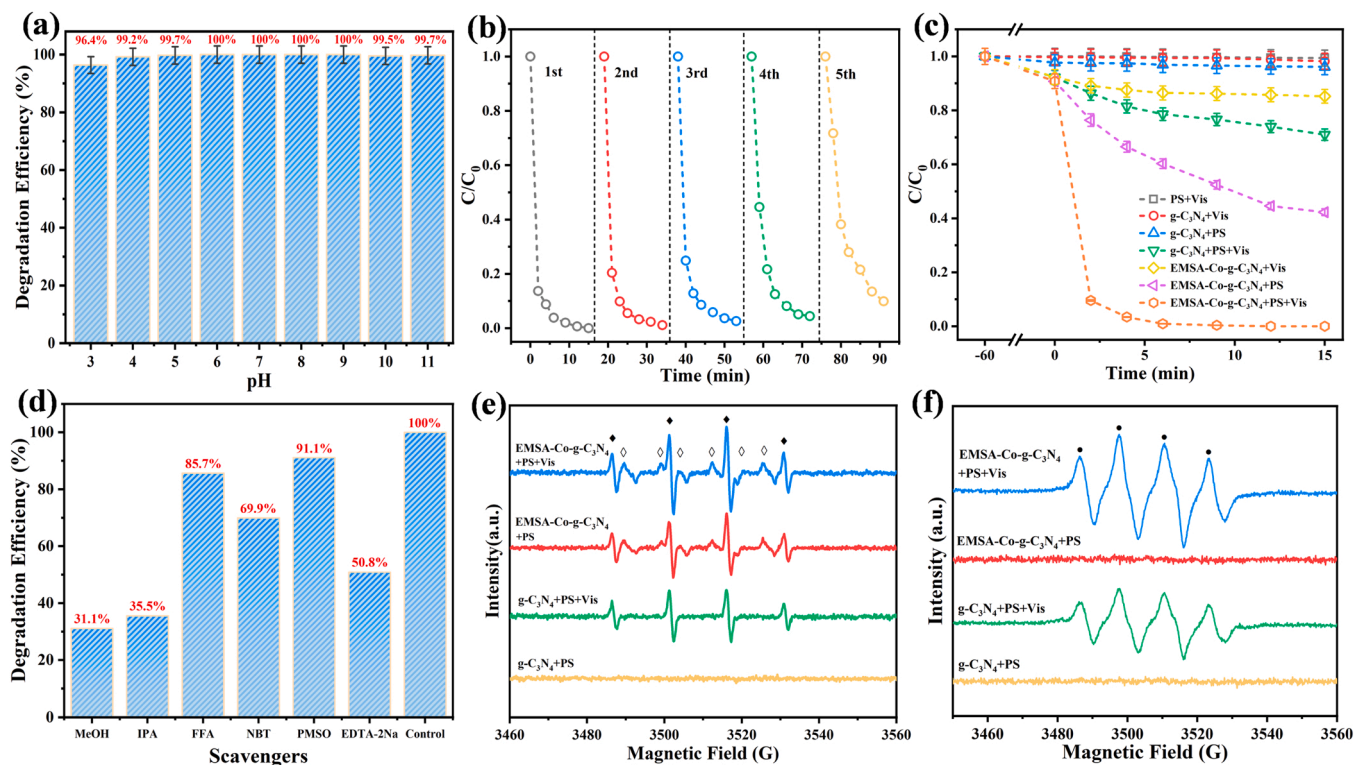
**Fig. 3.** (a) The effect of solution pH on the degradation of BPA and (b) cyclic degradation of BPA in the EMSA-Co-g-C$_3$N$_4$ +PS+Vis system. (c) Degradation of BPA in the various systems; and (d) Quench experiments for the degradation of BPA by the EMSA-Co-g-C$_3$N$_4$ under various quenching conditions. (e) EPR spectra of DMPO–•OH and DMPO–SO$_4^{\bullet-}$ in various systems (◆ represents DMPO–•OH, ◇ represents DMPO–SO$_4^{\bullet-}$). (f) EPR spectra of DMPO–O$_2^{\bullet-}$ in various systems (● represents DMPO–O$_2^{\bullet-}$) (Reaction condition: [catalyst] = 0.2 g/L, [PS] = 0.5 g/L, initial pH$_0$ = 7.0, [BPA] = 40.0 mg/L).

TBBPA and RhB with the removal percentages reached 98.5%, 100% and 100%, respectively. These results corroborate the excellent catalytic stability and performance of EMSA-Co-g-C$_3$N$_4$ for photo-Fenton-like reactions.

Fig. 3c shows that, under the same reaction conditions, the BPA degradation percentages reached 1.8% and 14.8% in g-C$_3$N$_4$+Vis and EMSA-Co-g-C$_3$N$_4$+Vis systems, respectively, suggesting the improved photocatalytic activity of EMSA-Co-g-C$_3$N$_4$. In heterogeneous g-C$_3$N$_4$+PS and EMSA-Co-g-C$_3$N$_4$+PS systems without light irradiation, BPA removal reached 3.9% and 57.7%, respectively, indicating the higher intrinsic catalytic activity of the implanted EMSA-Co single atom sites for PS activation. In addition, only 0.6% and 29.0% of BPA were degraded in the PS+Vis and the g-C$_3$N$_4$+PS+Vis systems, respectively, which indicates that PS cannot be activated by visible light or by g-C$_3$N$_4$ under visible light. In comparison, 100% of BPA was eliminated within 10 min in the EMSA-Co-g-C$_3$N$_4$+PS+Vis system, which could be due to the synergistically enhanced performance of photocatalytic and heterogenous PS activation mediated by the EMSA-Co sites. Kinetic plots of $-\ln(C/C_0)$ vs. t for the various systems are shown in Fig. S12, and the corresponding kinetic rate constants ($k(\min^{-1})$) are listed in Table S4. The $k$ value for EMSA-Co-g-C$_3$N$_4$+PS+Vis system is about 33, 12, 1180 and 55 times of that for g-C$_3$N$_4$+PS+Vis, EMSA-Co-g-C$_3$N$_4$+PS, g-C$_3$N$_4$+Vis and EMSA-Co-g-C$_3$N$_4$+Vis systems, respectively, verifying the superb catalytic performance of EMSA-Co-g-C$_3$N$_4$ for photo-Fenton-like reaction. As shown in Fig. S13, ~97% of BPA was eliminated from the spiked waste water treatment plant effluent, demonstrating its great potential for practical wastewater treatment. Moreover, the concentration of leached Co$^{2+}$ ions in the EMSA-Co-g-C$_3$N$_4$+PS+Vis system was measured to be ~55 ppb. As shown in Fig. S14, less than 3% of BPA was eliminated in the Co$^{2+}$/PMS system, demonstrating negligible contribution of the leached Co$^{2+}$ ions to BPA degradation. For comparison, the catalytic performances of Mn and Fe embedded in g-C$_3$N$_4$ (named as Mn-g-C$_3$N$_4$ and Fe-g-C$_3$N$_4$) were evaluated for BPA degradation. Details for

the fabrication and characterization of the Mn-g-C$_3$N$_4$ and Fe-g-C$_3$N$_4$ are shown in **Text S3**, Fig. S15 and S16. As shown in Fig. S17, the BPA degradation exhibited sluggish kinetics in the Mn-g-C$_3$N$_4$+PS+Vis and Fe-g-C$_3$N$_4$+PS+Vis systems with the BPA removal percentages reached 50.3% and 57.7%, respectively. As compared with the recently reported Co-based catalysts (Table S5), the EMSA-Co-g-C$_3$N$_4$ possesses much larger k-value for the degradation of BPA via PS or PMS activation. These results collectively demonstrate the high intrinsic catalytic activity of the EMSA-Co single sites for the heterogeneous Fenton-like reaction.

The produced ROS in the EMSA-Co-g-C$_3$N$_4$+PS+Vis system was probed by quenching experiments and EPR. Nitrotetrazolium blue chloride (NBT) for O$_2^{\bullet-}$, isopropanol (IPA) for •OH, methanol (MeOH) for both SO$_4^{\bullet-}$ and •OH, EDTA-2Na for holes, methyl phenyl sulfoxide (PMSO) for high valent Co species, and furfuryl alcohol (FFA) for $^1$O$_2$ were applied as the ROS scavengers. As revealed in Fig. 3d, only 35.5% and 31.1% of BPA was removed in the presence of IPA and MeOH, indicating SO$_4^{\bullet-}$ and •OH radicals had played the major roles in the catalytic oxidation process. The presence of FFA slightly prohibited BPA degradation, suggesting the insignificant role of $^1$O$_2$ for BPA oxidation. Meanwhile, after adding NBT into the EMSA-Co-g-C$_3$N$_4$+PS+Vis system, BPA removal was inhibited by ~30%, which suggests O$_2^{\bullet-}$ may also contribute to the degradation of BPA. The BPA removal was slightly inhibited by PMSO, demonstrating that the high valent Co species may not involve in the oxiation of BPA. In addition, BPA removal reached 50.8% in the presence of EDTA-2Na, indicating that the electron-holes may contribute to BPA degradation via the generation of ROSs. As shown in Fig. 3e, stronger EPR signals of SO$_4^{\bullet-}$ and •OH radicals can be observed in the EMSA-Co-g-C$_3$N$_4$+PS+Vis system, compared with the EMSA-Co-g-C$_3$N$_4$+PS system, verifying the enhanced PS activation and ROS generation by EMSA-Co-g-C$_3$N$_4$ under visible light. Moreover, the DMPO-SO$_4^{\bullet-}$ signals were observed in the EMSA-Co-g-C$_3$N$_4$+PS+Vis and EMSA-Co-g-C$_3$N$_4$+PS systems rather than in the g-C$_3$N$_4$+PS+Vis and g-

$C_3N_4$+PS systems, suggesting that the heterogeneous activation of PS was catalyzed by the EMSA-Co single-atom sites. Similarly, the DMPO-$O_2^{\bullet-}$ signals were observed only in the systems with visible light irradiation (Fig. 3 f and Fig. S18), which implies $O_2^{\bullet-}$ was generated by photocatalysis. In addition, feeble TEMP-$^1O_2$ signals can be found in the various catalytic systems due to the decomposition of the negligible quantity of PS (Fig. S19). These findings are consistent with the above quenching experiments. The results collectively verify that the EMSA-Co single-atom sites significantly boost the synergy between photocatalysis and heterogeneous Fenton-like reaction to realize the efficient generation of radical ROSs ($SO_4^{\bullet-}$, $\bullet OH$ and $O_2^{\bullet-}$), leading to enhanced degradation of BPA in the EMSA-Co-g-$C_3N_4$+PS+Vis system.

For a comprehensive understanding of BPA degradation pathways in the EMSA-Co-g-$C_3N_4$+PS+Vis system, the intermediate products were detected by LC-MS/MS (Fig. S20 and S21). The $P_2$ ($m/z = 317$) was produced via the coupling reactions between two BPA molecules. And then, the P2 was decomposed into $P_6$-$P_8$ by a series of ring-opening reactions [41]. The cleavage of the phenol groups resulted in the formation of $P_3$ ($m/z = 175$) and $P_4$ ($m/z = 133$) [42], and finally can be converted to $P_9$ ($m/z = 135$). At the same time, BPA can also be hydroxylated to produce $P_5$ ($m/z = 243$), then $P_{10}$ ($m/z = 241$) can be produced by dehydrogenation of $P_5$ [43]. Afterwards, $P_{10}$ ($m/z = 241$) can be oxidized into $P_{11}$ ($m/z = 249$). Both $P_9$ and $P_{11}$ can be converted to unstable hydroquinone ($P_{12}$, $m/z = 110$), and would be rapidly

oxidized into $P_{13}$ ($m/z = 108$) and $P_{14}$ ($m/z = 116$) [43]. At last, these intermediate products were mineralized to $CO_2$ and $H_2O$. As shown in Fig. S22, the removal of total organic carbon (TOC) reached 89.7% in the EMSA-Co-g-$C_3N_4$ +PS+Vis system, much higher than that in the g-$C_3N_4$ +PS+Vis system (12.7%), confirming the significant enhancement of BPA mineralization. Thus, the mechanisms for generation of ROSs and mineralization of BPA in the EMSA-Co-g-$C_3N_4$ +PS+Vis systems can be described by the following equations (Eqs. (1–7)) [44,45].
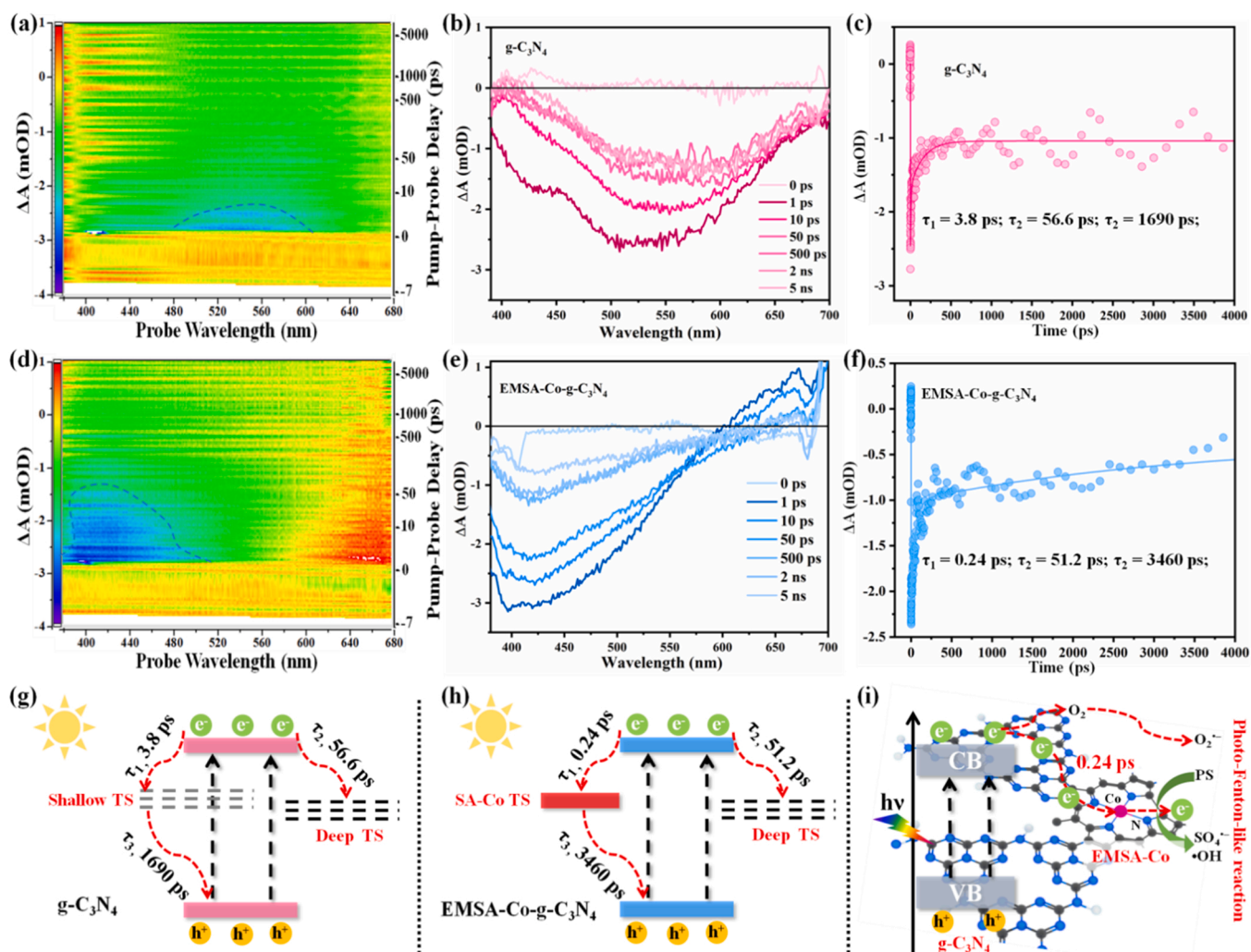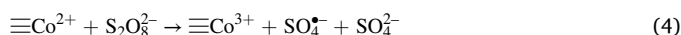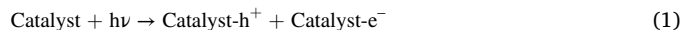
$$\text{Catalyst} + h\nu \rightarrow \text{Catalyst-}h^+ + \text{Catalyst-}e^- \tag{1}$$

$$O_2 + e^- \rightarrow O_2^{\bullet-} \tag{2}$$

$$H_2O + h^+ \rightarrow \bullet OH + H^+ \tag{3}$$

$$\equiv Co^{2+} + S_2O_8^{2-} \rightarrow \equiv Co^{3+} + SO_4^{\bullet-} + SO_4^{2-} \tag{4}$$

$$SO_4^{\bullet-} + H_2O \rightarrow SO_4^{2-} + \bullet OH + H^+ \tag{5}$$

$$\equiv Co^{3+} + e^- \rightarrow \equiv Co^{2+} \tag{6}$$

$$SO_4^{\bullet-} + \bullet OH + O_2^{\bullet-} + \text{BPA} \rightarrow \text{intermediates} \rightarrow CO_2 + H_2O \tag{7}$$



**Fig. 4.** (a) 2D TA spectrum, (b) TA spectra of g-$C_3N_4$ and (c) the corresponding TA kinetic at 480 nm. (d) 2D TA spectrum, (e) TA spectra of EMSA-Co-g-$C_3N_4$ and (f) the corresponding TA kinetic at 480 nm. Schematic depictions of the electron transfer process in (g) g-$C_3N_4$ and (h) EMSA-Co-g-$C_3N_4$. (i) Schematic illustration of directing and accelerating of the electron transfer by EMSA-Co sites for catalysis.

### 3.3. Charge transfer in EMSA-Co-g-C₃N₄

The charge carriers' dynamics were probed by femtosecond transient absorption (pump-probe) (fs-TA) spectroscopy. Upon 360 nm excitation (Fig. 4a and b), the fs-TA spectra of pure g-C₃N₄ exhibit continuous negative absorption in the range of 380–700 nm, which is due to the ground-state bleach and stimulated emission [46]. The corresponding fs-TA kinetic profiles of g-C₃N₄ at 480 nm are shown in Fig. 4c. As compared with pure g-C₃N₄, the fs-TA spectra of EMSA-Co-g-C₃N₄ manifest different absorption behaviors with negative absorption in the range of 380–600 nm and positive absorption in the range of 600–700 nm (Fig. 4d and e). The positive absorption is due to the hole-trapping, which is beneficial to separating charge carriers and eliminating the stimulated emission [47]. The absorption intensities of the fs-TA spectra decrease as a function of time, owing to the charge carrier recombination after the excitation [48]. Compared to g-C₃N₄, it takes a much longer time for the negative TA signals to decrease and reach to a steady value for EMSA-Co-g-C₃N₄, suggesting a longer lifetime of the electron-hole recombination [49]. In addition, EMSA-Co-g-C₃N₄ has higher fs-TA intensity than g-C₃N₄, suggesting its enhanced photocatalytic activity for producing more charge carriers [48]. The fs-TA kinetic profile of EMSA-Co-g-C₃N₄ at 480 nm is shown in Fig. 4 f. At the very beginning ($< 1$ ps), the fast decline in the kinetic profile is attributed to the initial generation and cooling of hot excitons, while the subsequent recovery (2–500 ps) is due to the exciton trapping processes [46,50]. First, electrons will be excited from valence band (VB) to conduction band (CB), leaving holes at the ground states. Subsequently, the excited electrons will relax to the VB edge to combine with holes or transfer to the nearby trap state (TS), and then fall back into the ground state [51]. The recombination of the electrons and holes usually happens in nanosecond (ns), while the charge transfer is much faster which occurs in picoseconds (ps) [51].

The fs-TA kinetics profiles were fitted by a tri-exponential function and the fitting parameters are $\tau_1 = 3.8$ ps, $\tau_2 = 56.6$ ps, $\tau_3 = 1690$ ps for pure C₃N₄, and $\tau_1 = 0.24$ ps, $\tau_2 = 51.2$ ps and $\tau_3 = 3460$ ps for EMSA-Co-g-C₃N₄. The corresponding electron-trapping models are schematically illustrated in Fig. 4 g and h for g-C₃N₄ and EMSA-Co-g-C₃N₄, respectively. For g-C₃N₄, the three components can be ascribed to the electrons transfer to shallow trapping state (TS) ($\tau_1 = 3.8$ ps), deep TS ($\tau_2 = 56.6$ ps) and the recombination of the shallow trapped electron with hole at the valence band (VB) ($\tau_3 = 1690$ ps), respectively [47]. The electron-trapping behavior of EMSA-Co-g-C₃N₄ is distinct from that of g-C₃N₄. For EMSA-Co-g-C₃N₄, the ultra-fast electron trapping process ($\tau_1 = 0.24$ ps) could be ascribed to electrons transfer to the trapping sites of the Co-corrin ring (Co-TS), owing to the presence of abundant C-vacancy in the strong π-conjugated system. The injected hot electrons may change the electronic distributions of the conjugated corrin-type CoN₄ sites and promote the redox circulation of the EMSA-Co sites. The slower electron-trapping process is assigned to the electrons transfer to the deep TS ($\tau_2 = 51.2$ ps) and the recombination of the trapped electron with hole ($\tau_3 = 3460$ ps), respectively [47]. The longer lifetime for the recombination of the electron/hole pairs in EMSA-Co-g-C₃N₄ suggests improved separation and migration of the photogenerated charge carriers. As illustrated in Fig. 4i, driven by the photogenerated electrons, the EMSA-Co-g-C₃N₄ exhibited an enhanced photo-Fenton-like reactivity for generating radical ROS. First, the enhanced photocatalysis of EMSA-Co-g-C₃N₄ promoted the reduction of dissolved oxygen to produce the $O_2^{\bullet-}$. Second, the Fenton-like reaction (PS activation) was boosted by directing and accelerating of electrons' transfer from photocatalytic g-C₃N₄ to the conjugated EMSA-Co sites, leading to efficient generation of $SO_4^{\bullet-}$ and •OH. As a result, the synergies between photocatalysis and heterogeneous Fenton-like reaction mediated by the EMSA-Co sites enhanced PS activation and ROS generation, giving rise to accelerated degradation of organic pollutants in the EMSA-Co-g-C₃N₄ +PS+Vis system.

The recombination of the photogenerated charge carrier was further probed by time-resolved PL decay spectra. As shown in Fig. 5a, the decay curves of g-C₃N₄ and EMSA-Co-g-C₃N₄ are fitted by a bi-exponential model, and the corresponding fitting parameters are shown in the inset table [28]. The average fluorescence lifetime ($\tau_{avg}$) for g-C₃N₄ and EMSA-Co-g-C₃N₄ are 3.1 and 6.1 ns, respectively. The prolonged PL decay lifetime indicates the reduced recombination and enhanced separation efficiency of the photoinduced charge carriers in EMSA-Co-g-C₃N₄.[52] These characters allowed EMSA-Co-g-C₃N₄ to supply more high-energy charge carriers migrating to catalyst surface for redox reactions. As shown in Fig. 5b, the photocurrent response for EMSA-Co-g-C₃N₄ was decreased with O₂ bubbling, owing to the consumption of photogenerated electrons by O₂ to produce less reactive and selective $O_2^{\bullet-}$ (–0.33 V). As compared with g-C₃N₄, the EMSA-Co-g-C₃N₄ exhibited an improved electron transfer capacity for sustained and steady PS activation, as observed from the i-t responses (Fig. 5c). These results confirm the efficient interfacial electron transfer of EMSA-Co-g-C₃N₄ to catalyze the photo-Fenton-like reaction.

From the density of states (PDOS) of EMSA-Co-g-C₃N₄ (Fig. 5d), an impurity bandgap between the Fermi level and the valence band (VB) was created, owing to the implanted EMSA-Co sites (Co-corrin ring) in g-C₃N₄. In addition, the Co 3d orbitals were hybridized with N 2p and C 2p orbitals at both VB and CB, suggesting the strong electronic interactions between the doped Co-corrin ring and the g-C₃N₄ substrate via the conjugated bonds, thereby facilitating electron transfer from the g-C₃N₄ substrate to the EMSA-Co single-atom sites [12]. Thus, the tailored electronic structure promotes EMSA-Co-g-C₃N₄ to produce more charge carriers with improved charge mobility [53]. The electronic location function (ELF) and Bader charge of EMSA-Co-g-C₃N₄ before and after injection of one electron were analyzed. As compared with pristine EMSA-Co-g-C₃N₄ (Fig. 5e and f), the injected electron was mainly distributed in the domain of the Co-corrin ring in EMSA-Co-g-C₃N₄, suggesting the efficient accumulation of the photogenerated electrons in the EMSA-Co sites. Bader charge analysis of EMSA-Co-g-C₃N₄ reveals the even charge delocalization in the Co-corrin ring (Fig. 5 g), owing to its strong conjugated structure. Whereas, after the injection of one electron, the charge distribution of Co-corrin ring was changed with more electron accumulation at the EMSA-Co site (Fig. 5j and S23), confirming the oriented accumulation of electrons at the EMSA-Co sites. These results collectively demonstrate the efficient separation and accumulation of electrons by EMSA-Co sites, thereby boosting its catalytic activity in the photo-Fenton-like reaction.

### 4. Conclusions

In conclusion, we have successfully synthesized cobalamin cofactor resembling Co–N₄ sites implanted in g-C₃N₄ via a facile copolymerization approach. The resultant EMSA-Co-g-C₃N₄ promoted the generation and migration of the photo-generated charge carriers, owing to strong coupling between the Co-corrin ring and the photocatalytic g-C₃N₄ via π-conjugated bonds. Moreover, fs-TA analysis and theoretical calculations demonstrated that the EMSA-Co sites were conducive to the separation and migration of photogenerated charge carriers, facilitating electron accumulation in the Co-corrin ring of EMSA-Co-g-C₃N₄ to accelerate the redox circulation of the Co single sites for PS activation. The EMSA-Co-g-C₃N₄ inherits high intrinsic catalytic activity of natural cobalamin enzyme and bridges photocatalysis and single-atom catalysis for PS activation, leading to efficient production of the radical species ($O_2^{\bullet-}$, $SO_4^{\bullet-}$, •OH) in the EMSA-Co-g-C₃N₄ +PS+Vis system. The photo-Fenton-like system mediated by EMSA-Co-g-C₃N₄ was proven to be effective in the removal of various organic pollutants from the aqueous solution. This study brings valuable insight into the application of enzyme-mimicking SACs for environmental remediation.

### CRediT authorship contribution statement

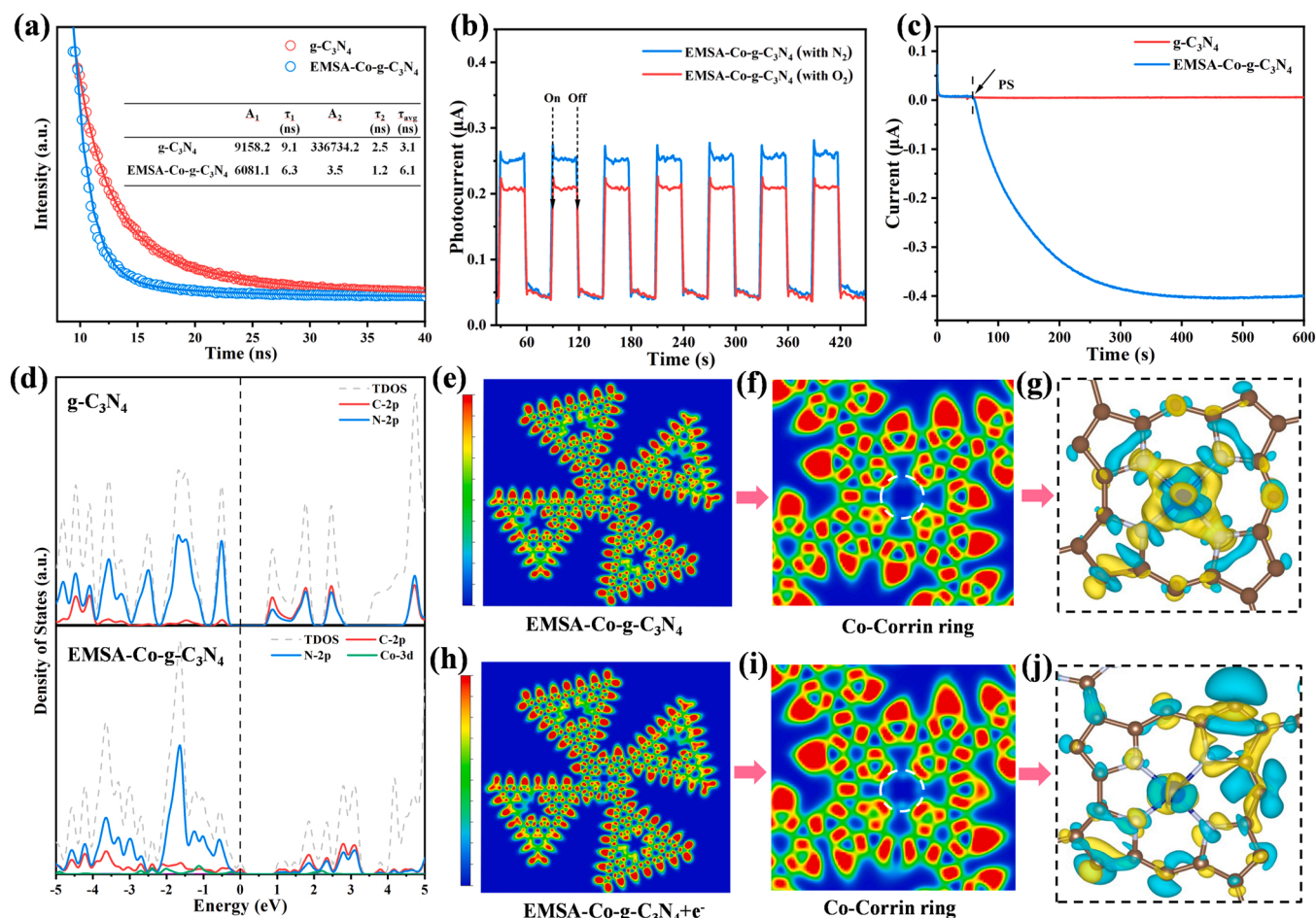**Shiang Liu**: Data curation, Formal analysis, Writing & editing.

**Fig. 5.** (a) Time-resolved transient photoluminescence (PL) spectra of g-C₃N₄ and EMSA-Co-g-C₃N₄. (b) Photocurrent response of EMSA-Co-g-C₃N₄ with O₂ or N₂ bubbling. (c) *i–t* curves of g-C₃N₄ EMSA-Co-g-C₃N₄ with the presence of PS. (d) PDOS of g-C₃N₄ and EMSA-Co-g-C₃N₄. (e) The electronic location function (ELF) of the EMSA-Co-g-C₃N₄, (f) the corresponding enlarged image and (g) Bader charge. (h) The electronic location function (ELF) of the EMSA-Co-g-C₃N₄ +e⁻, (f) the corresponding enlarged image and (g) Bader charge.

### Declaration of Competing Interest

The authors declare that they have no known competing financial interests or personal relationships that could have appeared to influence the work reported in this paper.

### Data Availability

Data will be made available on request.

### Appendix A. Supporting information

Supplementary data associated with this article can be found in the online version at doi:10.1016/j.apcatb.2023.122882.

### References

[1] C. Cai, H. Zhang, X. Zhong, L. Hou, Ultrasound enhanced heterogeneous activation of peroxymonosulfate by a bimetallic Fe-Co/SBA-15 catalyst for the degradation of Orange II in water, J. Hazard. Mater. 283 (2015) 70–79.

[2] W. Qin, G. Fang, Y. Wang, T. Wu, C. Zhu, D. Zhou, Efficient transformation of DDT by peroxymonosulfate activated with cobalt in aqueous systems: kinetics, products, and reactive species identification, Chemosphere 148 (2016) 68–76.

[3] H. Lee, H.-J. Lee, J. Jeong, J. Lee, N.-B. Park, C. Lee, Activation of persulfates by carbon nanotubes: oxidation of organic compounds by nonradical mechanism, Chem. Eng. J. 266 (2015) 28–33.

[4] Q. Yang, H. Choi, Y. Chen, D.D. Dionysiou, Heterogeneous activation of peroxymonosulfate by supported cobalt catalysts for the degradation of 2,4-dichlorophenol in water: the effect of support, cobalt precursor, and UV radiation, Appl. Catal. B: Environ. 77 (2008) 300–307.

[5] D. An, P. Westerhoff, M. Zheng, M. Wu, Y. Yang, C.-A. Chiu, UV-activated persulfate oxidation and regeneration of NOM-Saturated granular activated carbon, Water Res. 73 (2015) 304–310.

[6] Z. Wang, Y. Chen, P. Xie, R. Shang, J. Ma, Removal of microcystis aeruginosa by UV-activated persulfate: performance and characteristics, Chem. Eng. J. 300 (2016) 245–253.

[7] S. Wang, N. Zhou, Removal of carbamazepine from aqueous solution using sono-activated persulfate process, Ultrason. Sonochem. 29 (2016) 156–162.

[8] C. Tan, N. Gao, Y. Deng, N. An, J. Deng, Heat-activated persulfate oxidation of diuron in water, Chem. Eng. J. 203 (2012) 294–300.

[9] M. Marchesi, R. Aravena, K.S. Sra, N.R. Thomson, N. Otero, A. Soler, S. Mancini, Carbon isotope fractionation of chlorinated ethenes during oxidation by $Fe^{2+}$ activated persulfate, Sci. Total Environ. 433 (2012) 318–322.

[10] C.S. Liu, K. Shih, C.X. Sun, F. Wang, Oxidative degradation of propachlor by ferrous and copper ion activated persulfate, Sci. Total Environ. 416 (2012) 507–512.

[11] P. Wang, P. Xiao, S. Zhong, J. Chen, H. Lin, X.-L. Wu, Bamboo-like carbon nanotubes derived from colloidal polymer nanoplates for efficient removal of bisphenol A, J. Mater. Chem. A 4 (2016) 15450–15456.

[12] S. Liu, D. Liu, Y. Sun, P. Xiao, H. Lin, J. Chen, X.-L. Wu, X. Duan, S. Wang, Enzyme-mimicking single-atom $FeN_4$ sites for enhanced photo-Fenton-like reactions, Appl. Catal. B: Environ. 310 (2022), 121327.

[13] P. Avetta, A. Pensato, M. Minella, M. Malandrino, V. Maurino, C. Minero, K. Hanna, D. Vione, Activation of persulfate by irradiated magnetite: implications for the degradation of phenol under heterogeneous photo-Fenton-like conditions, Environ. Sci. Technol. 49 (2015) 1043–1050.

[14] Y. Tian, N. Jia, L. Zhou, J. Lei, L. Wang, J. Zhang, Y. Liu, Photo-Fenton-like degradation of antibiotics by inverse opal $WO_3$ co-catalytic $Fe^{2+}$/PMS, $Fe^{2+}$/$H_2O_2$ and $Fe^{2+}$/PDS processes: a comparative study, Chemosphere 288 (2022), 132627.

[15] S. Liang, C. Hao, Y. Shi, The power of single-atom catalysis, ChemCatChem 7 (2015) 2559–2567.

[16] F. Chen, X. Jiang, L. Zhang, R. Lang, B. Qiao, Single-atom catalysis: Bridging the homo- and heterogeneous catalysis, Chin. J. Catal. 39 (2018) 893–898.

[17] B. Qiao, A. Wang, X. Yang, L.F. Allard, Z. Jiang, Y. Cui, J. Liu, J. Li, T. Zhang, Single-atom catalysis of CO oxidation using $Pt_1$/$FeO_x$, Nat. Chem. 3 (2011) 634–641.

[18] A. Wang, J. Li, T. Zhang, Heterogeneous single-atom catalysis, Nat. Rev. Chem. 2 (2018) 65–81.

[19] C. Zhu, S. Fu, Q. Shi, D. Du, Y. Lin, Single-atom electrocatalysts, Angew. Chem. Int. Ed. 56 (2017) 13944–13960.

[20] H. Zhang, G. Liu, L. Shi, J. Ye, Single-atom catalysts: emerging multifunctional materials in heterogeneous catalysis, Adv. Energy Mater. 8 (2018), 1701343.

[21] C. Zhang, F. Li, R. Wen, H. Zhang, P. Elumalai, Q. Zheng, H. Chen, Y. Yang, M. Huang, G. Ying, Heterogeneous electro-Fenton using three-dimension NZVI-BC electrodes for degradation of neonicotinoid wastewater, Water Res. 182 (2020), 115975.

[22] R. Lang, X. Du, Y. Huang, X. Jiang, Q. Zhang, Y. Guo, K. Liu, B. Qiao, A. Wang, T. Zhang, Single-atom catalysts based on the metal-oxide interaction, Chem. Rev. 120 (2020) 11986–12043.

[23] Y.-W. Lin, Rational design of metalloenzymes: from single to multiple active sites, Coord. Chem. Rev. 336 (2017) 1–27.

[24] W. Wu, L. Huang, E. Wang, S. Dong, Atomic engineering of single-atom nanozymes for enzyme-like catalysis, Chem. Sci. 11 (2020) 9741–9756.

[25] L. Jiao, H. Yan, Y. Wu, W. Gu, C. Zhu, D. Du, Y. Lin, When nanozymes meet single-atom catalysis, Angew. Chem. Int. Ed. 132 (2020) 2585–2596.

[26] M. Koutmos, S. Datta, K.A. Pattridge, J.L. Smith, R.G. Matthews, Insights into the reactivation of cobalamin-dependent methionine synthase, Proc. Natl. Acad. Sci. USA 106 (2009) 18527–18532.

[27] W. Song, P. Ge, Q. Ke, Y. Sun, F. Chen, H. Wang, Y. Shi, X.-L. Wu, H. Lin, J. Chen, C. Shen, Insight into the mechanisms for hexavalent chromium reduction and sulfisoxazole degradation catalyzed by graphitic carbon nitride: the Yin and Yang in the photo-assisted processes, Chemosphere 221 (2019) 166–174.

[28] H. Zhang, J. Lin, Z. Li, T. Li, X. Jia, X.-L. Wu, S. Hu, H. Lin, J. Chen, J. Zhu, Organic dye doped graphitic carbon nitride with a tailored electronic structure for enhanced photocatalytic hydrogen production, Catal. Sci. Technol. 9 (2019) 502–508.

[29] I. Papailias, T. Giannakopoulou, N. Todorova, D. Demotikali, T. Vaimakis, C. Trapalis, Effect of processing temperature on structure and photocatalytic properties of g-$C_3N_4$, Appl. Surf. Sci. 358 (2015) 278–286.

[30] X. Cai, A. Wang, J. Wang, R. Wang, S. Zhong, Y. Zhao, L. Wu, J. Chen, S. Bai, Order engineering on the lattice of intermetallic PdCu co-catalysts for boosting the photocatalytic conversion of $CO_2$ into $CH_4$, J. Mater. Chem. A 6 (2018) 17444–17456.

[31] H. Yu, R. Shi, Y. Zhao, T. Bian, Y. Zhao, C. Zhou, G.I.N. Waterhouse, L.-Z. Wu, C.-H. Tung, T. Zhang, Alkali-assisted synthesis of nitrogen deficient graphitic carbon nitride with tunable band structures for efficient visible-light-driven hydrogen evolution, Adv. Mater. 29 (2017), 1605148.

[32] W. Che, W. Cheng, T. Yao, F. Tang, W. Liu, H. Su, Y. Huang, Q. Liu, J. Liu, F. Hu, Z. Pan, Z. Sun, S. Wei, Fast photoelectron transfer in ($C_{ring}$)-$C_3N_4$ plane

[33] X. Xu, T. Wang, W. Lu, L. Dong, H. Zhang, X. Miao, $Co_xP$@$Co_3O_4$ nanocomposite on cobalt foam as efficient bifunctional electrocatalysts for hydrazine-assisted hydrogen production, ACS Sustain. Chem. Eng. 9 (2021) 4688–4701.

[34] K. Wang, Y. Liu, Z. Ding, Z. Chen, X. Xu, M. Wang, T. Lu, L. Pan, Chloride pre-intercalated CoFe-layered double hydroxide as chloride ion capturing electrode for capacitive deionization, Chem. Eng. J. 433 (2022), 133578.

[35] Y. Zheng, L. Zhang, H. Huang, F. Wang, L. Yin, H. Jiang, D. Wang, J. Yang, G. Zuo, ZIF-67-derived Co, Ni and S co-doped N-enriched porous carbon polyhedron as an efficient electrocatalyst for oxygen evolution reaction (OER), Int. J. Hydrog. Energy 44 (2019) 27465–27471.

[36] W. Liu, L. Zhang, W. Yan, X. Liu, X. Yang, S. Miao, W. Wang, A. Wang, T. Zhang, Single-atom dispersed Co-N-C catalyst: structure identification and performance for hydrogenative coupling of nitroarenes, Chem. Sci. 7 (2016) 5758–5764.

[37] Z. Du, X. Chen, W. Hu, C. Chuang, S. Xie, A. Hu, W. Yan, X. Kong, X. Wu, H. Ji, L. J. Wan, Cobalt in nitrogen-doped graphene as single-atom catalyst for high-sulfur content lithium-sulfur batteries, J. Am. Chem. Soc. 141 (2019) 3977–3985.

[38] G. Liu, P. Niu, C. Sun, S.C. Smith, Z. Chen, G.Q. Lu, H.-M. Cheng, Unique electronic structure induced high photoreactivity of sulfur-doped graphitic $C_3N_4$, J. Am. Chem. Soc. 132 (2010) 11642–11648.

[39] G. Zhang, M. Zhang, X. Ye, X. Qiu, S. Lin, X. Wang, Iodine modified carbon nitride semiconductors as visible light photocatalysts for hydrogen evolution, Adv. Mater. 26 (2014) 805–809.

[40] T. Sano, S. Tsutsui, K. Koike, T. Hirakawa, Y. Teramoto, N. Negishi, K. Takeuchi, Activation of graphitic carbon nitride (g-$C_3N_4$) by alkaline hydrothermal treatment for photocatalytic NO oxidation in gas phase, J. Mater. Chem. A 1 (2013) 6489–6496.

[41] Y. Zhu, D. Li, S. Zuo, Z. Guan, S. Ding, D. Xia, X. Li, $Cu_2O$/CuO induced non-radical/radical pathway toward highly efficient peroxymonosulfate activation, J. Environ. Chem. Eng. 9 (2021), 106781.

[42] Q. Wang, Y. Cao, Y. Yu, C. Zhang, J. Huang, G. Liu, X. Zhang, Z. Wang, H. Ozgun, M.E. Ersahin, W. Wang, Enhanced visible-light driven photocatalytic degradation of bisphenol A by tuning electronic structure of Bi/BiOBr, Chemosphere 308 (2022), 136276.

[43] Q. Wang, Z. Xu, Y. Cao, Y. Chen, X. Du, Y. Yang, Z. Wang, Two-dimensional ultrathin perforated $Co_3O_4$ nanosheets enhanced PMS-Activated selective oxidation of organic micropollutants in environmental remediation, Chem. Eng. J. 427 (2022), 131953.

[44] R. Yin, W. Guo, H. Wang, J. Du, Q. Wu, J.-S. Chang, N. Ren, Singlet oxygen-dominated peroxydisulfate activation by sludge-derived biochar for sulfamethoxazole degradation through a nonradical oxidation pathway: performance and mechanism, Chem. Eng. J. 357 (2019) 589–599.

[45] A. Fazli, A. Khataee, M. Brigante, G. Mailhot, Cubic cobalt and zinc co-doped magnetite nanoparticles for persulfate and hydrogen peroxide activation towards the effective photodegradation of Sulfalene, Chem. Eng. J. 404 (2021) 126391.

[46] C. Zhao, Z. Chen, J. Xu, Q. Liu, H. Xu, H. Tang, G. Li, Y. Jiang, F. Qu, Z. Lin, X. Yang, Probing supramolecular assembly and charge carrier dynamics toward enhanced photocatalytic hydrogen evolution in 2D graphitic carbon nitride nanosheets, Appl. Catal. B: Environ. 256 (2019), 117867.

[47] J. Chang, G. Wang, Y. Yang, Recent advances in electrode design for rechargeable zinc–air batteries, Small Sci. 1 (2021), 2100044.

[48] W. Lei, Y. Mi, R. Feng, P. Liu, S. Hu, J. Yu, X. Liu, J.A. Rodriguez, J.-O. Wang, L. Zheng, K. Tang, S. Zhu, G. Liu, M. Liu, Hybrid 0D–2D black phosphorus quantum dots–graphitic carbon nitride nanosheets for efficient hydrogen evolution, Nano Energy 50 (2018) 552–561.

[49] C. Zhao, L. Tian, Z. Zou, Z. Chen, H. Tang, Q. Liu, Z. Lin, X. Yang, Revealing and accelerating interfacial charge carrier dynamics in Z-scheme heterojunctions for highly efficient photocatalytic oxygen evolution, Appl. Catal. B: Environ. 268 (2020), 118445.

[50] Z. Chen, Q. Zhang, Y. Luo, Experimental identification of ultrafast reverse hole transfer at the interface of the photoexcited methanol/graphitic carbon nitride system, Angew. Chem. Int. Ed. 57 (2018) 5320–5324.

[51] X. Jin, L. Zhang, X. Fan, J. Tian, M. Wang, J. Shi, A photo-excited electron transfer hyperchannel constructed in Pt-dispersed pyrimidine-modified carbon nitride for remarkably enhanced water-splitting photocatalytic activity, Appl. Catal. B: Environ. 237 (2018) 888–894.

[52] Z. Li, Y. Wu, G. Lu, Highly efficient hydrogen evolution over $Co(OH)_2$ nanoparticles modified g-$C_3N_4$ co-sensitized by Eosin Y and rose bengal under visible light irradiation, Appl. Catal. B: Environ. 188 (2016) 56–64.

[53] X.-H. Jiang, L.-S. Zhang, H.-Y. Liu, D.-S. Wu, F.-Y. Wu, L. Tian, L.-L. Liu, J.-P. Zou, S.-L. Luo, B.-B. Chen, Silver single atom in carbon nitride catalyst for highly efficient photocatalytic hydrogen evolution, Angew. Chem. Int. Ed. 132 (2020) 23312–23316.